Chinese Chemical Letters 37 (2026) 111346

Contents lists available at ScienceDirect

Chinese Chemical Letters

journal homepage: www.elsevier.com/locate/cclet

Aggregation-enhanced antenna effects of dynamic chiral Eu(III) complexes significantly enhance imaging of living cells and zebrafish

Hai-Ling Wang[a,*], Bing Yu[b], Fu-Pei Liang[b], Hua-Hong Zou[b,*]

[a] School of Chemistry and Chemical Engineering, Guangxi Key Laboratory of Electrochemical Energy Materials, Guangxi University, Nanning 530004, China
[b] Key Laboratory for Chemistry and Molecular Engineering of Medicinal Resources (Ministry of Education of China), Guangxi Key Laboratory of Chemistry and Molecular Engineering of Medicinal Resources, School of Chemistry and Pharmaceutical Sciences, Guangxi Normal University, Guilin 541004, China

ARTICLE INFO

Article history:
Received 1 April 2025
Revised 9 May 2025
Accepted 19 May 2025
Available online 19 May 2025

Keywords:
Dynamic chiral Eu(III) complexes
Antenna effect
Aggregation-induced emission
Bioimaging
Solvothermal synthesis

ABSTRACT

In this work, the aggregation-enhanced antenna effect of chiral mononuclear Eu(III) complexes containing dynamic modules in aqueous solution was used for the first time to significantly improve the optical imaging performance of various types of cells and zebrafish. Specifically, the chiral mononuclear Eu(III) complexes (***R/S*-1** and ***R/S*-2**) containing molecular rotors or vibration unit modules have almost negligible emission in the molecule state, but after aggregation in aqueous solution, they form nanoparticles with a sharp increase in emission peaks. It is worth noting that the above photophysical properties lead to ***R/S*-1** and ***R/S*-2** having high-resolution cell imaging effects on various cells, and localizing in lysosomal organelles. In addition, ***R/S*-1** and ***R/S*-2** also show high-resolution optical imaging effects on zebrafish. This work not only opens a door to expand the bioimaging performance of lanthanide complex emitters but also opens a new perspective for the construction of new dynamic lanthanide complexes with bright emissions.

© 2026 Published by Elsevier B.V. on behalf of Chinese Chemical Society and Institute of Materia Medica, Chinese Academy of Medical Sciences.

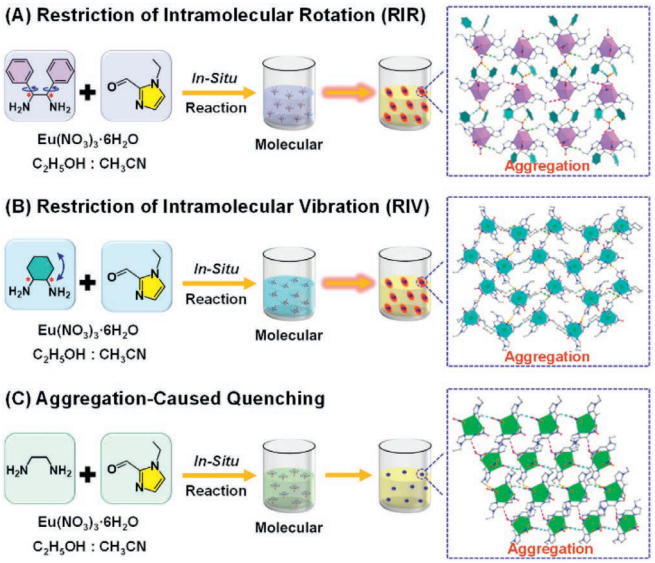
The special electronic configuration of lanthanide ions leads to a series of advantages of lanthanide complex emitters, such as pure color, large Stokes shift, and long lifetime, and has become an ideal choice for 3D high-definition display, information storage, encryption, solid-state lighting and bioimaging [1–6]. Among the various lanthanide complex emitters, chiral Eu(III) complexes with strong luminescence behavior and excellent circularly polarized luminescence (CPL) performance are dazzling [7–9]. This is mainly because the $^5D_0 \rightarrow {}^7F_1$ energy level transition of Eu(III) ions belongs to the D^1-type transition that can induce chiral Eu(III) complexes to have a high luminescence asymmetry factor (g_{lum}) [10–14]. Although the optical applications of these chiral Eu(III) complexes have made considerable progress in solid-state and non-aqueous solvents, their applications in water systems (*e.g.*, bioimaging) have made almost no progress [15,16]. There are two main reasons: (1) The characteristic emission of Eu(III) ions is very susceptible to the vibration-quenching effect of H_2O [2]. (2) After the Eu(III) complex aggregates form nanoparticles in an aqueous solution, the changes in the conformation, stacking, and arrangement of the ligands can easily lead to the failure of the antenna effect and cause luminescence quenching behavior [17].

Aggregation-induced emission luminogens (AIEgens) containing molecular rotors or vibrational units have shown great application prospects in high-resolution bioimaging, photodynamic therapy, and immunotherapy due to the bright emission caused by the aggregation effect in aqueous solution [18–20]. Traditional AIEgens are mainly organic fluorophores containing molecular rotors or vibrational modules, and lanthanide complexes with aggregation-enhanced luminescence behavior are very rare [21–26]. In 2024, Zou research group used chiral ligands containing molecular rotors and vibrational units to synthesize dynamic chiral mononuclear Eu(III) complexes with aggregation-enhanced antenna effect behavior under solvothermal conditions and achieved a double enhancement of g_{lum} value (0.64) and luminescence brightness (B_{CPL} value, 2429 L mol^{-1} cm^{-1}) [27]. After the Eu(III) complex aggregates to form nanoparticles in an aqueous solution, the tight stacking of the outer layer of the Eu(III) complex molecules can effectively block the internal complex molecules from being attacked by H_2O, and can also weaken the vibration quenching effect of H_2O on its characteristic emission. So far, chiral Eu(III) complexes that can show obvious aggregation-enhanced antenna effects in aqueous systems have not been reported.

Herein, we have used the restriction of intramolecular rotation (RIR) and restriction of intramolecular vibration (RIV) mechanisms to achieve the aggregation-enhanced antenna effect of dynamic chiral mononuclear Eu(III) complexes (***R/S*-1** and ***R/S*-2**) in aque-

* Corresponding authors.
E-mail addresses: whl2016010984@163.com (H.-L. Wang), gxnuchem@foxmail.com (H.-H. Zou).

https://doi.org/10.1016/j.cclet.2025.111346
1001-8417/© 2026 Published by Elsevier B.V. on behalf of Chinese Chemical Society and Institute of Materia Medica, Chinese Academy of Medical Sciences.



Scheme 1. Schematic diagram of the one-pot synthesis of lanthanide complexes with different optical properties using dynamic chiral ligands with (A) molecular rotors or (B) vibration units and (C) traditional ligands.

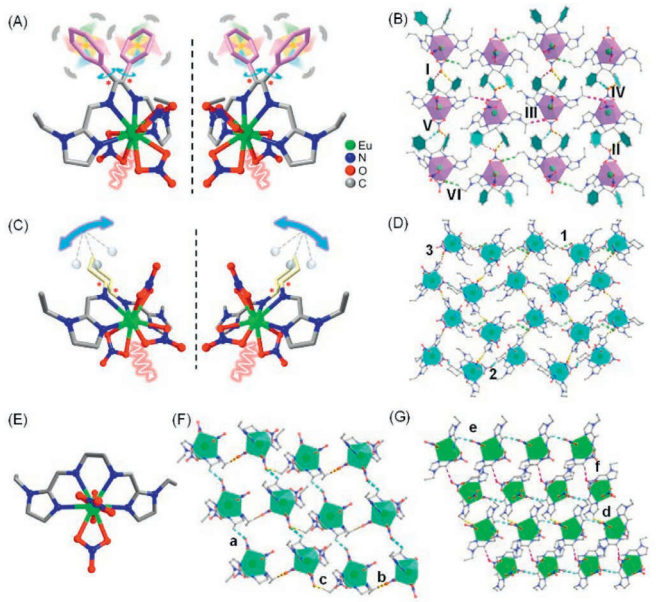


Fig. 1. (A) Crystal structures of complexes ***R*-1** (left) and ***S*-1** (right). (B) Strong hydrogen bonding interactions between molecules of complex ***R*-1**. (C) Crystal structures of complexes ***R*-2** (left) and ***S*-2** (right). (D) Strong hydrogen bonding interactions between molecules of complex ***R*-2**. (E) Crystal structure of achiral complex **3**. (F, G) Strong hydrogen bonding interactions between molecules of complex **3**.

ous solution for the first time, resulting in a dramatic increase in red characteristic luminescence and high-resolution optical imaging of living cells and zebrafish (Scheme 1). The structure of the enantiomer ***R*/*S*-1**, which relies on the RIR mechanism for luminescence enhancement, contains a freely rotatable molecular rotor. In the single-molecule state, the free rotation dissipates the energy of the excited state and shows almost negligible luminescence behavior. In the aggregated state, the molecular rotor structure of ***R*/*S*-1** is locked by hydrogen bonds and steric effects and cannot rotate freely, which enhances the antenna effect and leads to a sharp increase in the emission peak. Similarly, the structure of ***R*/*S*-2**, which relies on the RIV mechanism, contains a cyclohexane core structure that can undergo configuration switching. The configuration switching of cyclohexane in the single-molecule state induces significant vibration, thereby dissipating the energy of the excited state. After aggregation in an aqueous solution, strong hydrogen bonding interactions restrict the configuration-switching behavior of cyclohexane, thereby enhancing the characteristic emission of Eu(III) ions. Based on the above photophysical properties, ***R*/*S*-1** and ***R*/*S*-2** have high-resolution optical imaging effects on a variety of different types of cancer cells or normal cells, and can effectively mark the lysosomal organelles of these cells. In addition, the bright characteristic emission of Eu(III) ions of ***R*/*S*-1** and ***R*/*S*-2** in aqueous solution can also effectively mark the yolk sac and liver of zebrafish embryos and larvae. Cell and *in vivo* experiments of ***R*/*S*-1** and ***R*/*S*-2** have proved that they have excellent biosafety. This work not only provides a new method for constructing dynamic lanthanide complex emitters with bright emission but also opens a door for the bioimaging application of lanthanide complex emitters in aqueous solution.

Based on our previous work, 1-ethyl-1*H*-imidazole-2-carbaldehyde (0.1 mmol), (1*R*/*S*,2*R*/*S*)-(-/+)-1,2-diphenylethylenediamine (0.1 mmol) and $Eu(NO_3)_3{\cdot}6H_2O$ (0.1 mmol) were dissolved in a mixed solvent of EtOH:CH_3CN = 1:1, and reacted under solvothermal conditions at 80 °C for 24 h to obtain two pale yellow block crystals ***R*/*S*-1** [27]. Only by replacing (1*R*/*S*,2*R*/*S*)-(-/+)-1,2-diphenylethylenediamine with a molecular rotor structure with (1*R*/*S*,2*R*/*S*)-(-/+)-1,2-cyclohexanediamine containing a vibration unit structure, another pair of pale yellow block crystals ***R*/*S*-2** were obtained. The large-scale synthesis of simple Eu(III) complexes ***R*/*S*-1** and ***R*/*S*-2** can be easily achieved by scaling up the reaction (Fig. S1 in Supporting information). In addition, the achiral ethylenediamine was further replaced with (1*R*/*S*,2*R*/*S*)-(-/+)-1,2-diphenylethylenediamine containing a molecular rotor structure to obtain a pale yellow block crystal **3**. Single crystal X-ray diffraction (SCXRD) showed that ***R*/*S*-1** was crystallized in the orthorhombic system of the $P2_12_12_1$ chiral space group. Enantiomers ***R*/*S*-1** are composed of a Eu(III) ion, a chiral Schiff base ligand (*R*/*S*-L^1, L^1 = (1*E*,1′*E*)-*N*,*N*′-(1,2-diphenylethane-1,2-diyl)bis(1-(1-ethyl-1*H*-imidazol-2yl)methanimine)) and three terminal-coordinated NO_3^- ions, and their molecular formula is [Eu(*R*/*S*-L^1)$(NO_3)_3$]. Obviously, in the single-molecule state of the complex ***R*/*S*-1**, the molecular rotor in the *R*/*S*-L^1 ligand in the structure can rotate freely, similar to a "windmill", and can effectively rotate and dissipate energy (Fig. 1A). The molecular rotor in the structure of the complex ***R*/*S*-1** in the aggregated state is locked by the significant steric effect of the adjacent molecules and the strong hydrogen bond interaction, and the rotation of the molecular rotor is greatly restricted. Specifically, the complex ***R*/*S*-1** is connected by six different strong hydrogen bonds (I, $C_{13}-H_{13}\cdots O_{15}$ (2.5538 Å); II, $C_{20}-H_{20}\cdots O_{15}$ (2.4928 Å); III, $C_{23}-H_{23B}\cdots O_4$ (2.5377 Å); IV, $C_{39}-H_{39}\cdots O_6$ (2.5139 Å); V, $C_{46}-H_{46}\cdots O_6$ (2.0541 Å) and VI, $C_{50}-H_{50C}\cdots O_{13}$ (2.5534 Å)) in the aggregated state to form a three-dimensional stacking structure (Fig. 1B and Table S1 in Supporting information). Enantiomers ***R*/*S*-2** are all crystallized in the $P2_12_12_1$ chiral space group of the orthorhombic system. The complexes ***R*/*S*-2** are composed of a Eu(III) ion, a chiral Schiff base ligand (*R*/*S*-L^2, L^2 = (1*E*,1′*E*)-*N*,*N*′-(cyclohexane-1,2-diyl)bis(1-(1-ethyl-1*H*-imidazol-2-yl)methanimine)) and three terminal-coordinated NO_3^- ions, and their molecular formula is [Eu(*R*/*S*-L^2)$(NO_3)_3$]·CH_3CN. Due to the steric hindrance effect, the ligand *R*/*S*-L^2 in the structure of the complex ***R*/*S*-2** can have obvious vibrations in the single molecule state (Fig. 1C). Obviously, in the aggregated state, the molecules of complex ***R*/*S*-2** also have obvious strong hydrogen bond interactions (1, $C_9-H_{9A}\cdots O_2$ (3.0604 Å); 2, $C_8-H_{8B}\cdots O_8$ (2.8409 Å); and 3, $C_{17}-H_{17}\cdots O_2$ (3.0531 Å)) (Fig. 1D and Table S1). These hydrogen bonds effectively lock the vibration unit, fix the

molecular conformation of ***R/S*-2**, and greatly restrict the vibration of cyclohexane in *R/S*-L^2 ligand. SCXRD shows that the non-chiral complex **3** crystallizes in the $P-1$ space group of the triclinic system. Complex **3** is composed of a Eu(III) ion, a Schiff base ligand (L^3, L^3 = (1*E*,1′*E*)-*N*,*N*'-(ethane-1,2-diyl)bis(1(1-ethyl-1*H*-imidazol-2-yl)methanimine)) and three terminal-coordinated NO_3^- ions, and its molecular formula is [Eu(L^3)(NO_3)$_3$] (Fig. 1E). Six different hydrogen bonds (a, $C_{21}-H_{21B}\cdots O_4$ (2.8602 Å); b, $C_{30}-H_{30A}\cdots O_{13}$ (2.7341 Å); c, $C_{33}-H_{33B}\cdots O_4$ (2.8372 Å); d, $C_{14}-H_{14}\cdots O_6$ (2.4614 Å); e, $C_{19}-H_{19}\cdots O_8$ (2.4844 Å) and f, $C_{24}-H_{24}\cdots O_{13}$ (2.7539 Å)) connect the independent units of complex **3** to form a three-dimensional stacking structure (Figs. 1F and G, Table S1). Based on the above series of structural foundations, it can be seen that the movement of the molecular rotors and vibration units of complexes ***R/S*-1** and ***R/S*-2** in the aggregated state is significantly restricted, which is expected to show obvious aggregation-induced emission behavior, thus having special optical properties. The powder X-ray diffraction results (PXRD) show that the observed values of complexes ***R/S*-1**, ***R/S*-2**, and **3** are highly consistent with their simulated values, proving that they are all pure phases (Fig. S2 in Supporting information). The characteristic absorption peaks of the Fourier transform infrared absorption (FTIR) spectra of complexes ***R/S*-1**, ***R/S*-2**, and **3** are consistent with the functional groups in the structure (Fig. S3 in Supporting information). Thermogravimetric (TG) analysis of complexes ***R/S*-1**, ***R/S*-2**, and **3** is shown in Fig. S4 (Supporting information), which identifies the solvent guest molecules in the structures of these complexes. High-resolution transmission electron microscopy (HRTEM) proves that complexes ***R/S*-1**, ***R/S*-2**, and **3** are all block crystals with very clean surfaces (Fig. S5 in Supporting information). In addition, X-ray energy dispersion spectroscopy (EDS) shows that all elements in the structures of complexes ***R/S*-1**, ***R/S*-2**, and **3** are uniformly distributed (Fig. S5).

Lanthanide complex emitters with excellent photophysical properties and bright emission have shown great application prospects in solid-state lighting, sensing, optical coding, and bioimaging [1,28–32]. However, there are still few examples of the application of lanthanide complex emitters in solution, especially aqueous solution [15,16]. The main reason is that most lanthanide complexes have poor stability, solubility, or dispersibility in aqueous solution, and the characteristic emission of lanthanide ions is easily affected by the vibration quenching effect of X-H (X = C, N, O) [17]. In addition, the highly exposed metal cluster core of lanthanide complex emitters is easy to binds to macromolecules in living systems, such as proteins and DNA, thus showing non-negligible biological toxicity [33–35]. Based on the obvious molecular rotors and vibration unit modules in the structures of complexes ***R/S*-1** and ***R/S*-2**, we believe that they can show obvious aggregation-enhanced antenna effect behavior after aggregation in an aqueous solution, thereby showing significantly enhanced characteristic emission. To verify our hypothesis, ***R/S*-1** and ***R/S*-2** were dispersed in H_2O under irradiation of a 365 nm UV lamp, and the solution showed bright red light, while no significant luminescence behavior was shown when dispersed in DMSO. These significant luminescence differences confirmed our hypothesis. Specifically, with DMSO as a good solvent and H_2O as a poor solvent, the same amount of ***R/S*-1** and ***R/S*-2** was dissolved in H_2O/DMSO mixed solutions with different H_2O contents (f_w), and the emission spectra of the above series of mixed solutions were tested (Figs. 2A-E). The experimental results show that with the increase of the content of good solvent (DMSO), the emission intensity of ***R/S*-1** and ***R/S*-2** at 592/593, 617/619, and 651 nm gradually weakened. With the increase of the content of poor solvent (H_2O), the emission intensity of ***R/S*-1** and ***R/S*-2** showed a significant enhancement trend, and the emission intensity reached the maximum value when the content of poor solvent H_2O reached 90 % or 99 %, proving that ***R/S*-1** and ***R/S*-2** both showed significant AIE characteristics (Figs. 2F-J). No obvious regular changes were observed in complex **3** without molecular rotors or vibration units under the same mixed solvent conditions, and the red emission disappeared significantly when the content of poor solvent reached 99 %, proving that complex **3** showed significant aggregation-induced luminescence quenching (ACQ) effect in aqueous solution. In addition, the UV–visible absorption spectra of ***R/S*-1**, ***R/S*-2**, and **3** in 99 % H_2O or DMSO were tested (Figs. 2K-O). The experimental results show that with the increase of the proportion of poor solvent, the UV-visible absorption of ***R/S*-1**, ***R/S*-2**, and **3** all produced obvious redshifts and tail absorptions higher than the origin, indicating that they formed nano aggregates in the poor solvent H_2O. Complexes ***R/S*-1**, ***R/S*-2**, and **3** all showed characteristic fingerprint emission peaks at 592, 617, and 651 nm, which were attributed to the $^5D_0 \rightarrow {}^7F_1$, $^5D_0 \rightarrow {}^7F_2$ and $^5D_0 \rightarrow {}^7F_3$ energy level transitions of Eu(III) ions, respectively (Fig. S6 in Supporting information) [21–24]. In addition, the luminescence lifetimes of complexes ***R/S*-1**, ***R/S*-2**, and **3** were 192.3, 190.0, 438.2, 396.7, and 245.8 μs, respectively (Fig. S7 in Supporting information), and the luminescence quantum yields of complexes ***R/S*-1** and ***R/S*-2** were 25.10 %, 21.99 %, 18.27 % and 18.38 %, respectively (Table S2 in Supporting information).

The AIE characteristics of ***R/S*-1** and ***R/S*-2** can be explained by the RIR and RIV mechanisms, respectively. For ***R/S*-1** containing molecular rotors, in the single-molecule state, the excited electrons mainly dissipate energy and return to the ground state through the non-radiative transition pathway caused by the movement of the molecular rotor. In the aggregated state, the movement of the molecular rotors in the *R/S*-L^1 ligands in the structure of the complex ***R/S*-1** is hindered by the steric hindrance of the adjacent molecules and the locking of the strong hydrogen bond interaction. The excited electrons are dominated by radiative transitions, which promote the ISC process, enhance the antenna effect, and ultimately enhance the radiative transitions of Eu(III) ions. Similarly, for the complex ***R/S*-2** containing vibration units, in the single-molecule state, the cyclohexane on the *R/S*-L^2 ligand can produce free vibrations through configuration changes, and the energy of the excited state returns to the ground state in a non-radiative transition manner to dominate. In the aggregated state, the configuration switching of cyclohexane in the *R/S*-L^2 ligand is restricted due to the strong hydrogen bonding interaction, which promotes the ISC process and enhances the energy transfer (ET) pathway to effectively transfer more energy to the Eu(III) ion, thereby enhancing its characteristic fingerprint emission peak. In addition, equal amounts of ***R/S*-1**, ***R/S*-2**, and **3** were dispersed in a mixed solvent ($V_{DMSO}/V_{water} = 1/99$), and the hydration diameters of the above complexes were obtained by dynamic light scattering (DLS) to be 121.9, 104.2, 205.4, 375.6 and 101.2 nm, respectively (Figs. 2P-T). The above results prove that these complexes can form stable aggregates in an aqueous solution and have highly uniform nanometer sizes. The energy transfer pathway and luminescence mechanism of the complex's ***R/S*-1** and ***R/S*-2** were further analyzed using the Jablonsky energy level diagram. According to the results of our reported work, the energy gaps between the first excited singlet state (S_1) and the first excited triplet state (T_1) of the organic ligands *R/S*-L^1 and *R/S*-L^2 are 7149 and 8169 cm^{-1}, respectively. According to Reinhold's rule of thumb, when the energy gap between S_1 and T_1 is greater than 5000 cm^{-1}, the ISC process can be effectively realized. In addition, the energy gaps between the T_1 state energy level of the ligands *R/S*-L^1 and *R/S*-L^2 and the lowest excited state energy level ($^5D_0$ energy level) of the Eu(III) ion are 2525 and 3066 cm^{-1}, respectively, which conforms to Latva's rule of thumb, proving that the ligands *R/S*-L^1 and *R/S*-L^2 have a high degree of energy level matching with the Eu(III) ion and efficient energy transfer, and can serve as efficient antennas (Fig. S6F).

After aggregation in aqueous solution, traditional lanthanide complexes are prone to aggregation-caused quenching (ACQ) due

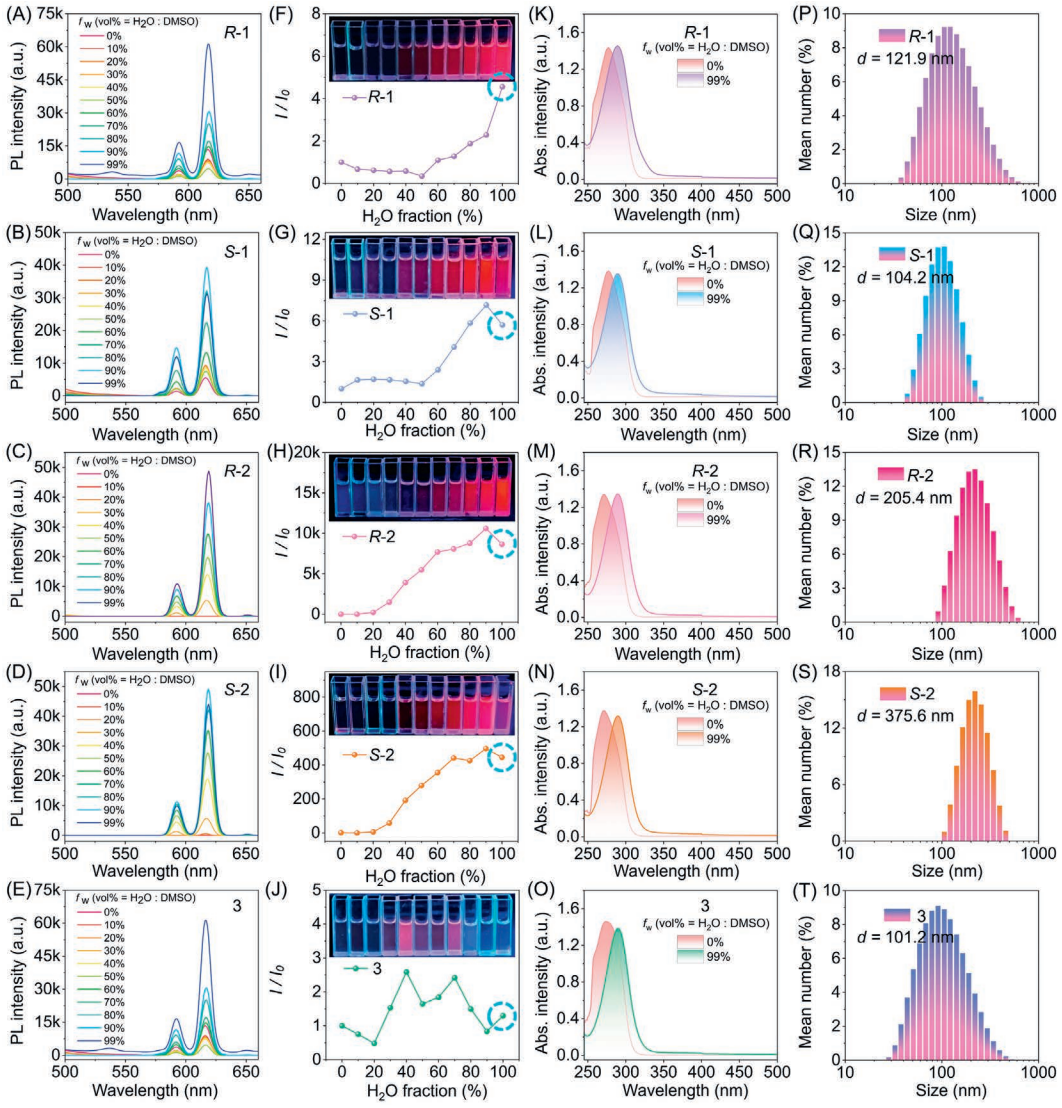


Fig. 2. Emission spectra of complexes (A) ***R*-1**, (B) ***S*-1**, (C) ***R*-2**, (D) ***S*-2** and (E) **3** in mixed solutions of H_2O/DMSO with different contents under 344 nm excitation; Variation of the intensity of the emission peak at 617 nm of complexes (F) ***R*-1**, (G) ***S*-1**, (H) ***R*-2**, (I) ***S*-2** and (J) **3** with f_w, the inset shows the luminescence photos of ***R*-1**, ***S*-1**, ***R*-2**, ***S*-2** and **3** in mixed solutions of H_2O/DMSO with different ratios, note: The blue dotted circle indicates the emission peak intensity enhancement factor in a mixed solution of 99 % H_2O and 1 % DMSO. UV-visible absorption spectra of complexes (K) ***R*-1**, (L) ***S*-1**, (M) ***R*-2**, (N) ***S*-2** and (O) **3** in mixed solutions of H_2O/DMSO with different f_w contents; DLS results of complexes (P) ***R*-1**, (Q) ***S*-1**, (R) ***R*-2**, (S) ***S*-2** and (T) **3** in a mixed solution of H_2O/DMSO = 1:99.

to changes in ligand conformation, and the characteristic luminescence of lanthanide ions is easily affected by the vibrational quenching effect caused by water or hydroxyl groups [2]. In addition, traditional lanthanide complexes have highly exposed metal centers, which have obvious biological toxicity and very low aqueous solution stability [15,16]. Therefore, high-resolution biological imaging of lanthanide complexes has progressed slowly. Based on the significant AIE behavior of complexes ***R*/*S*-1** and ***R*/*S*-2** in aqueous solution, it is obvious that they have broad application prospects in the field of high-performance biological imaging. The stability of ***R*/*S*-1**, ***R*/*S*-2** and **3** in mixed solvents ($V_{DMSO}/V_{water} = 1/99$) was explored using zeta potential, and the results showed that the absolute values of their zeta potentials were 40.4, 56.9, 35.6, 70.2 and 66.9 mV, respectively (Fig. 3A). In addition, complexes ***R*/*S*-1**, ***R*/*S*-2** and **3** were able to maintain high stability after being dispersed in water, PBS, and cell culture medium (DMEM) for 5 days, respectively (Fig. S8 in Supporting information). Complexes ***R*-1** and ***R*-2** are both stable in aqueous solutions containing Ca^{2+}, Zn^{2+}, and Mg^{2+} ions, respectively (Fig. S9 in Supporting information), indicating that these complexes have high stability in aqueous solutions containing endogenous metal ions, further laying the foundation for their application *in vivo* imaging. The above results demonstrate that the nano aggregates formed by these complexes in aqueous solution are very stable.

The cytotoxicity of complexes ***R*/*S*-1**, ***R*/*S*-2** and **3** on HeLa and 4T1 cells was evaluated by MTT colorimetry. The experimental results showed that after incubation of HeLa or 4T1 cells with ***R*/*S*-1**, ***R*/*S*-2** and **3** solutions of different concentrations (0, 6.25, 12.5, 25, 50, 100 μg/mL) for 12 h, the survival rates of 4T1 (Fig. 3B and Fig. S10 in Supporting information) and HeLa (Fig. S11 in Supporting information) cells were all higher than 70 %, indicating that the cytotoxicity of these complexes was negligible. Based on the highly uniform nanosize, high water stability, and low cytotoxicity of complexes ***R*/*S*-1**, ***R*/*S*-2** and **3**, their applications in cell imaging were further explored. HeLa and 4T1 cells were cultured in an incubator at 37 °C and 5 % CO_2, and allowed to attach and grow until the density of the confocal dish reached 90 %. 5 μL of 10 mg/mL ***R*/*S*-1**, ***R*/*S*-2** and **3** solution was incubated with HeLa and 4T1

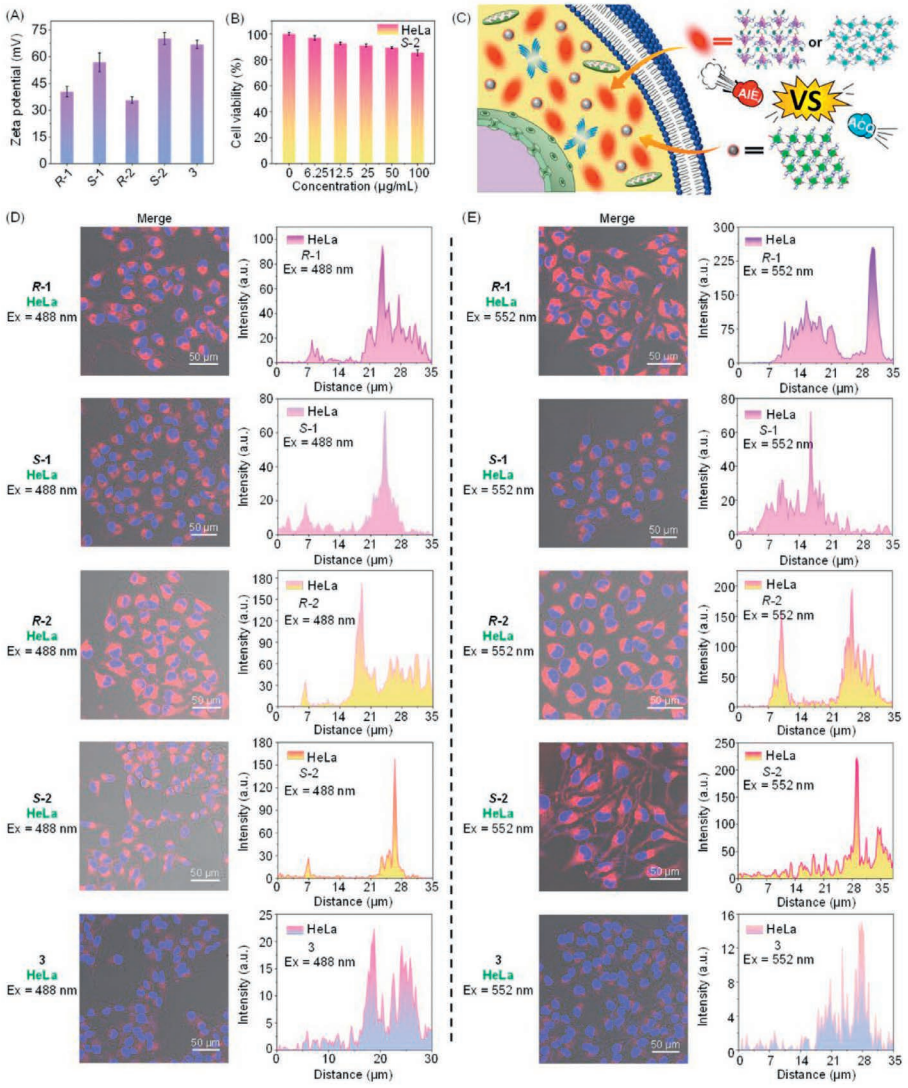


Fig. 3. (A) Zeta potential of complexes ***R*-1**, ***S*-1**, ***R*-2**, ***S*-2** and **3** after forming nano aggregates in aqueous solution. (B) MTT assay to monitor the growth inhibition rate of 4T1 cells with different concentrations of ***S*-2**. (C) Schematic diagram of cell imaging of lanthanide complexes with AIE and ACQ properties; CLSM images and fluorescence intensity quantitative analysis results of complexes ***R*-1**, ***S*-1**, ***R*-2**, ***S*-2** and **3** after incubation with HeLa cells at excitation wavelengths of (D) 488 nm and (E) 552 nm.

cells for 12 h, and the above cells were imaged *in vitro* by two-photon laser confocal microscopy (CLSM). The *in vitro* imaging results showed that the complexes ***R*/*S*-1** and ***R*/*S*-2** could efficiently label HeLa and 4T1 cells, and showed bright red light in the cytoplasm. However, complex **3** showed negligible labeling ability for the above cells, and there was almost no obvious red light in the cytoplasm (Fig. 3C). The fluorescence intensity of the individual cells of the above cells was quantitatively analyzed, and the analysis results showed that the fluorescence intensity of the complexes ***R*/*S*-1** and ***R*/*S*-2** in HeLa and 4T1 cells was 2.6 to 6.7 times that of complex **3**, which was consistent with the phenomenon observed by our naked eyes (Figs. 3D and E, Figs. S12-S15 in Supporting information). After ***R*-1** and ***R*-2** were co-incubated with HepG2 cells, MDA-MB-231 cells, and WI-38 cells, they were effectively taken up by HepG2 cells, MDA-MB-231 cells, and WI-38 cells, and showed bright red luminescence in these cells, proving that ***R*-1** and ***R*-2** can effectively label the above cells (Figs. S16-S18 in Supporting information). The classic AIEgen, tetraphenylethylene (TPE), was selected for cell imaging comparison. The results showed that under the same concentration and incubation time, the uptake and fluorescence intensity of TPE in HeLa cells were significantly lower than those of ***R*-1** and ***R*-2** (Fig. S19 in Supporting information), proving the great application prospects of lanthanide complexes with aggregation-enhanced antenna effect in the field of biological imaging. The AIE effect of complexes ***R*/*S*-1** and ***R*/*S*-2** in aqueous solution leads to their excellent fluorescence imaging effect on cells. According to the distribution of ***R*/*S*-1** and ***R*/*S*-2** in cells, it is preliminarily judged that the organelles specifically labeled are lysosomes (Fig. 4). To further determine the localization of complexes ***R*-1** and ***R*-2** in cells, they were co-localized with the commercial lysosomal probe LysoTracker Green (Figs. 4A and B). The co-localization results showed that the luminescent areas of complexes ***R*-1**, ***R*-2**, and lysosomal probes in cells were highly overlapped, proving that they can specifically label lysosomes. As far as we know, this is one of the rare examples of lanthanide complex emitters with AIE properties in the field of biological fluorescence imaging, opening up new horizons for the development of new biological imaging probes.

Based on the excellent *in vitro* cell imaging effect and biocompatibility of the complex's ***R*/*S*-1** and ***R*/*S*-2**, their performance *in vivo* imaging was further explored. Zebrafish embryos and larvae have the advantages of high transparency of tissues and organs, less light scattering and absorption in their bodies, and high homology between genes and human genes, which are suitable for

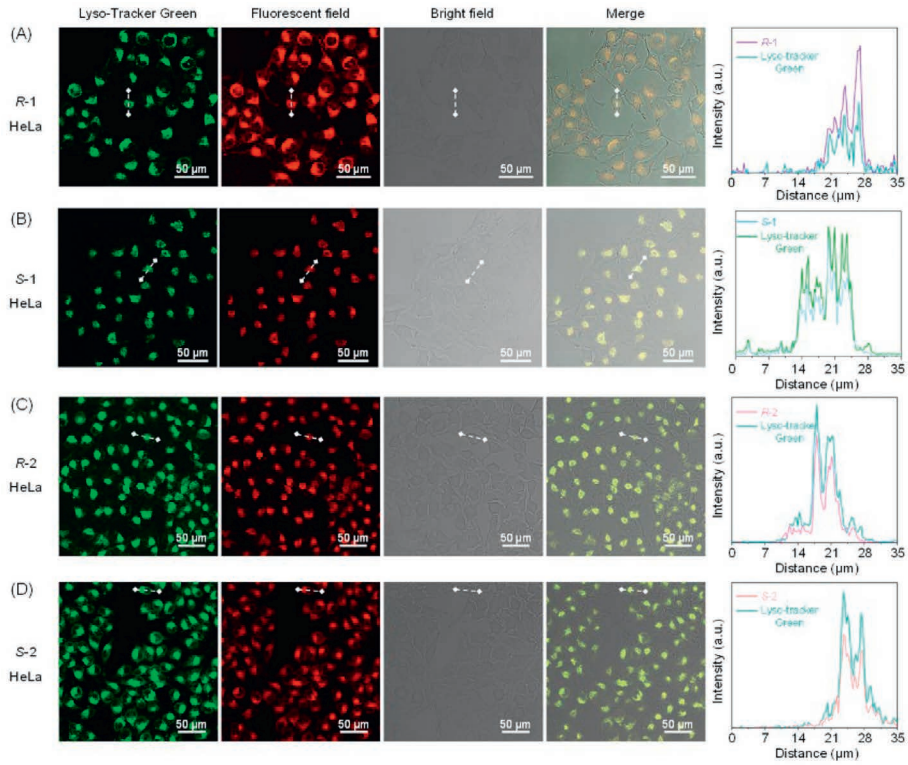


Fig. 4. CLSM images of ***R*-1** (A), ***S*-1** (B), ***R*-2** (C), ***S*-2** (D) and LysoTracker Green (Beyotime Biotechnology) localized on the lysosomes of HeLa; Quantitative analysis of the fluorescence intensity of ***R*-1**, ***S*-1**, ***R*-2**, ***S*-2** and LysoTracker Green in HeLa cells.

biological imaging. ***R/S*-1** and ***R/S*-2** at a concentration of 50 μg/mL were incubated with zebrafish embryos and larvae at 48 hpf after fertilization for 1, 2, 3, 6, and 12 h, respectively, and the *in vivo* imaging effect of the above zebrafish embryos and larvae was evaluated by two-photon laser confocal microscopy (CLSM). The results of embryo imaging experiments showed that after incubation with ***R/S*-1** and ***R/S*-2** for 1 h, ***R/S*-1** and ***R/S*-2** could be effectively taken up by the embryos through the villi and distributed in the embryonic eggshell. After 2 h of incubation, the eggshell and yolk sac regions of the embryo showed weak red luminescence, and as the incubation time increased, the red luminescence gradually increased and spread throughout the zebrafish embryo (Fig. 5). The embryos were re-hatched and the imaging experiment of zebrafish larvae was performed after the embryos developed into early larval morphology. The experimental results showed that ***R/S*-1** and ***R/S*-2** could be effectively ingested by larvae and mainly distributed in the yolk sac and liver regions. The fluorescence intensity of the main organs of zebrafish embryos and larvae was further statistically analyzed, and the results showed that the imaging effect of ***R*-1** in zebrafish embryos was better than that of ***R*-2**, while the imaging effect of ***R*-2** in zebrafish larvae was better than that of ***R*-1** (Figs. S20 and S21 in Supporting information). As the incubation time increased, the red luminescence in the larvae gradually increased, which was confirmed by the fluorescence quantitative analysis of the larvae (Fig. 5, Figs. S22 and S23 in Supporting information).

The biosafety of ***R*-1** and ***R*-2** in mice was further evaluated. The results of hemolysis experiments and H&E staining of major organ sections showed that ***R*-1** and ***R*-2** did not cause obvious tissue toxicity and could be administered by tail vein injection (Figs. S24 and S25 in Supporting information), proving that ***R*-1** and ***R*-2** had good biosafety. Obviously, by introducing dynamic ligands containing molecular rotors or vibration units into lanthanide complexes, the aggregation effect can be used to effectively promote the "antenna effect" and improve the luminescence performance of lanthanide complexes. As far as we know, this is the first time that lanthanide complexes with aggregation-enhanced antenna effects have been applied to high-resolution bioimaging, which opens a door for the development of dynamic lanthanide complexes in the field of bioimaging.

In summary, dynamic chiral mononuclear Eu(III) complexes (***R/S*-1** and ***R/S*-2**) containing molecular rotors or vibrational units realize the aggregation-enhanced antenna effect in aqueous solution by restriction of intramolecular motion (RIM) mechanism and obtain optical imaging applications of living cells and zebrafish with high resolution. The enantiomer ***R/S*-1** with obvious molecular rotor structure presents a single molecule state in a DMSO solution with negligible luminescence, while it presents a nano-aggregated state with bright red luminescence in a mixed solution containing 99% H_2O and 1% DMSO. The reason for the sharp increase of the emission peak of ***R/S*-1** in aqueous solution is mainly due to the strong hydrogen bonding locking effect and steric hindrance effect leading to the restriction of intramolecular rotation (RIR) of the molecular rotor in the structure. Similarly, ***R/S*-2** containing vibrational unit modules also shows bright red emission in aqueous solution due to the restriction of intramolecular vibration (RIV) caused by strong hydrogen bonding and steric hindrance effect. Complex **3** without molecular rotor or vibrational unit structure shows an obvious ACQ effect with the change of the ratio of DMSO and H_2O. Based on the above photophysical properties, the chiral enantiomers ***R/S*-1** and ***R/S*-2** have high-resolution optical imaging effects on various types of living cells and are localized in lysosomal organelles. In addition, isomers ***R/S*-1** and ***R/S*-2** also have high-definition fluorescence imaging effects on zebrafish, mainly distributed in the yolk sac and liver regions of zebrafish embryos and larvae. To the best of our knowledge, this is the first time that the RIR and RIV mechanisms are used to realize the aggregation-enhanced antenna effect of dynamic mononu-

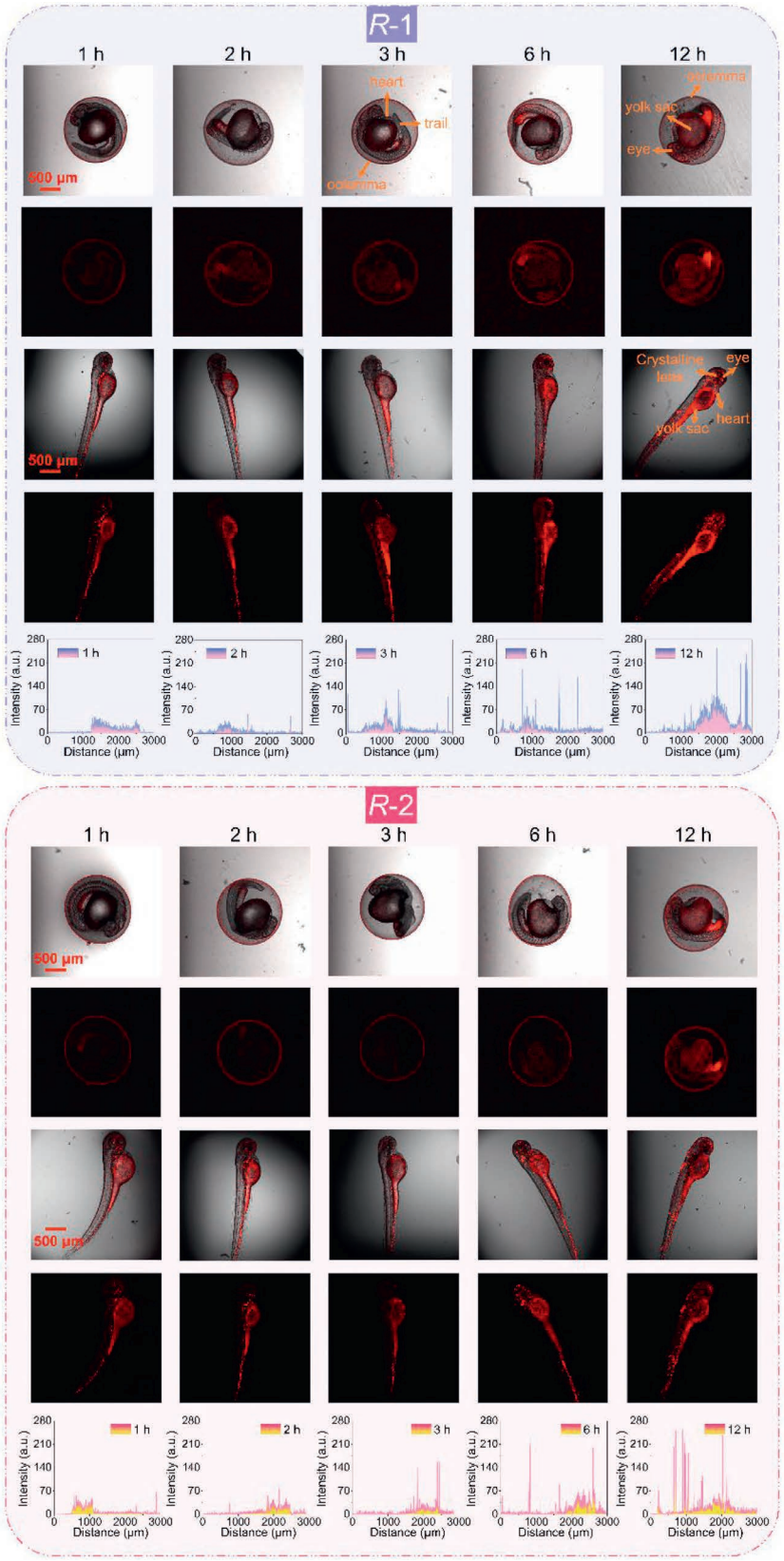


Fig. 5. CLSM images and fluorescence intensity quantitative analysis results of ***R*-1** and ***R*-2** co-incubated with zebrafish embryos and larvae for 1, 2, 3, 6, and 12 h, respectively.

clear Eu(III) complexes in aqueous systems, and high-performance *in vitro* and *in vivo* fluorescence imaging effects have been obtained. This work not only develops a new method for constructing lanthanide complex emitters with bright emission in aqueous solution but also opens a new blueprint for the application of lanthanide complex emitters in the field of high-resolution biological imaging.

CRediT authorship contribution statement

Hai-Ling Wang: Writing – review & editing, Writing – original draft, Visualization, Validation, Supervision, Project administration, Methodology, Investigation, Funding acquisition, Formal analysis, Conceptualization. **Bing Yu:** Writing – original draft, Software, Methodology, Formal analysis, Data curation. **Fu-Pei Liang:** Visualization, Validation, Project administration, Methodology, Funding acquisition. **Hua-Hong Zou:** Writing – review & editing, Validation, Supervision, Methodology, Funding acquisition.

Declaration of competing interest

The authors declare that they have no known competing financial interests or personal relationships that could have appeared to influence the work reported in this paper.

Acknowledgments

This work was supported by the Startup Fund of Guangxi University (No. ZX1080030424008), the Natural Science Foundation of Guangxi (No. 2025GXNSFDA069029), the Guangxi University Young and Middle-aged Teachers' Scientific Research Basic Capacity Improvement Project (No. 2025KY0054), and the National Natural Science Foundation of China (No. 22061005).

Supplementary materials

Supplementary material associated with this article can be found, in the online version, at doi:10.1016/j.cclet.2025.111346.

References

[1] X.Z. Li, C.B. Tian, Q.F. Sun, Chem. Rev. 122 (2022) 6374–6458.
[2] Y. Yang, X. Hu, Z. Yang, W. Huang, Adv. Funct. Mater. 35 (2025) 2412970.
[3] J.H. Jia, Q.W. Li, Y.C. Chen, J.L. Liu, M.L. Tong, Coord. Chem. Rev. 378 (2019) 365–381.
[4] T. Xian, Q. Meng, F. Gao, M. Hu, X. Wang, Coord. Chem. Rev. 474 (2023) 214866.
[5] P.P. Ferreira da Rosa, Y. Kitagawa, Y. Hasegawa, Coord. Chem. Rev. 406 (2020) 213153.
[6] R. Xue, Y.S. Liu, W. Yang, G.Y. Yang, Coord. Chem. Rev. 501 (2024) 215577.
[7] C. Zhang, S. Zhao, M.M. Zhang, et al., Coord. Chem. Rev. 514 (2024) 215859.
[8] A.G. Bispo-Jr, N.A. Oliveira, I.M.S. Diogenis, F.A. Sigoli, Coord. Chem. Rev. 523 (2025) 216279.
[9] Y. Zhao, J. Li, C. Zhan, Sci. Sin. Chim. 54 (2024) 1212–1232.
[10] J. Pang, Z. Yao, K. Zhang, et al., Angew. Chem. Int. Ed. 62 (2023) e202217456.
[11] S.J. Hu, X.Q. Guo, L.P. Zhou, et al., J. Am. Chem. Soc. 144 (2022) 4244–4253.
[12] Y. Zhou, H. Li, T. Zhu, T. Gao, P. Yan, J. Am. Chem. Soc. 141 (2019) 19634–19643.
[13] Y.B. Tan, Y. Okayasu, S. Katao, et al., J. Am. Chem. Soc. 142 (2020) 17653–17661.
[14] M. Tsurui, R. Takizawa, Y. Kitagawa, et al., Angew. Chem. Int. Ed. 63 (2024) e202405584.
[15] H. Wang, Z. Ni, Z. Ruan, et al., Nano Res. 16 (2023) 11495–11502.
[16] B. Yu, Z.H. Zhu, W.W. Qin, et al., ACS Mater. Lett. 6 (2024) 3312–3326.
[17] P. Su, T. Wang, P. Zhou, et al., Natl. Sci. Rev. 9 (2022) nwab016.
[18] J. Mei, N.L.C. Leung, R.T.K. Kwok, J.W.Y. Lam, B.Z. Tang, Chem. Rev. 115 (2015) 11718–11940.
[19] G. Feng, G.Q. Zhang, D. Ding, Chem. Soc. Rev. 49 (2020) 8179–8234.
[20] X. Feng, X. Wang, C. Redshaw, B.Z. Tang, Chem. Soc. Rev. 52 (2023) 6715–6753.
[21] Y. Kong, Z. Yan, S. Li, et al., Angew. Chem. Int. Ed. 59 (2020) 5336–5340.
[22] D.A. Gálico, M. Murugesu, Angew. Chem. Int. Ed. 61 (2022) e202204839.
[23] E.V. Salerno, A.N. Carneiro Neto, S.V. Eliseeva, et al., J. Am. Chem. Soc. 144 (2022) 18259–18271.
[24] M.Y. Ye, M.X. Zhang, Q.F. Xu, et al., Sci. China Chem. 66 (2023) 1400–1405.
[25] M. Zhang, X. Dong, Z. Wang, et al., Angew. Chem. Int. Ed. 59 (2020) 10052–10058.
[26] Y.Y. Liu, X. Zhang, K. Li, et al., Angew. Chem. Int. Ed. 60 (2021) 22417–22423.
[27] Y.L. Li, H.L. Wang, Z.H. Zhu, et al., Nat. Commun. 15 (2024) 2896.
[28] Z. Li, F. Jiang, M. Yu, et al., Nat. Commun. 13 (2022) 2142.
[29] Y.L. Li, H.L. Wang, Z.C. Chen, et al., Chem. Eng. J. 451 (2023) 138880.
[30] W.W. Qin, H.L. Wang, Y.L. Li, et al., ACS Mater. Lett. 6 (2024) 4911–4921.
[31] R. Wang, H. Zhang, S. Wang, et al., Inorg. Chem. Front. 10 (2023) 1534–1542.
[32] S. Wang, B. Sun, J. Sun, et al., Dye. Pigment. 223 (2024) 111930.
[33] I. Martinić, S.V. Eliseeva, T.N. Nguyen, V.L. Pecoraro, S. Petoud, J. Am. Chem. Soc. 139 (2017) 8388–8391.
[34] D.T. Thielemann, A.T. Wagner, E. Rösch, et al., J. Am. Chem. Soc. 135 (2013) 7454–7457.
[35] H.L. Wang, D. Liu, J.H. Jia, et al., Natl. Sci. Rev. 10 (2023) nwad036.